

FAST Adaptive Smoothing and Thresholding for Improved Activation Detection in Low-Signal fMRI

Israel Almodóvar-Rivera and Ranjan Maitra

Abstract

Functional Magnetic Resonance Imaging is a noninvasive tool used to study brain function. Detecting activation is challenged by many factors, and even more so in low-signal scenarios that arise in the performance of high-level cognitive tasks. We provide a fully automated and fast adaptive smoothing and thresholding (FAST) algorithm that uses smoothing and extreme value theory on correlated statistical parametric maps for thresholding. Performance on simulation experiments spanning a range of low-signal settings is very encouraging. The methodology also performs well in a study to identify the cerebral regions that perceive only-auditory-reliable and only-visual-reliable speech stimuli as well as those that perceive one but not the other.

Index Terms

AM-FAST, AR-FAST, Adaptive Segmentation, AFNI, BIC, circulant matrix, CNR, Cluster Thresholding, Gumbel distribution, SNR, SPM, SUMA, reverse Weibull distribution

I. INTRODUCTION

FUNCTIONAL Magnetic Resonance Imaging (fMRI) [1]–[9] studies the spatial characteristics and extent of brain function while at rest or, more commonly, while performing tasks or responding to external stimuli. In the latter scenario, which is the setting for this paper, the imaging modality acquires voxel-wise Blood-Oxygen-Level-Dependent (BOLD) measurements [10], [11] at rest and during stimulation or performance of a task. After pre-processing, a statistical model such as a general linear model [4], [12] is fit to the time course sequence against the expected BOLD response [13]–[15]. Statistical Parametric Mapping (SPM) [16] techniques provide voxel-wise test statistics summarizing the association between the time series response at that voxel and the expected BOLD response [3]. The map of test statistics is then thresholded to identify significantly activated voxels [17]–[19].

The analysis of fMRI datasets is challenged [20]–[23] by factors such as scanner, inter- and intra-subject variability, voluntary/involuntary or stimulus-correlated motion and also the several-seconds delay in the BOLD response while the neural stimulus passes through the hemodynamic filter [23]–[25]. Pre-processing steps [22], [26] mitigate some of these effects, but additional challenges are presented by the fact that an fMRI study is expected to have no more than 1-3% activated voxels [8], [27]. Also, many activation studies involving high-level cognitive processes have low contrast-to-noise ratios (CNR), throwing up more issues as illustrated next.

A. Activation Detection during Noisy Audiovisual Speech

The most important way in which humans communicate is through speech [28]–[30], which the brain is particularly adept at understanding, even when this form of communication is degraded by noise. It is

I. Almodóvar-Rivera is with the Department of Biostatistics and Epidemiology at the University of Puerto Rico, Medical Science Campus, San Juan, Puerto Rico, USA.

R.Maitra is with the Department of Statistics, Iowa State University, Ames, Iowa, USA.

This research was supported in part by the National Institute of Biomedical Imaging and Bioengineering (NIBIB) of the National Institutes of Health (NIH) under its Award No. R21EB016212. I. Almodóvar-Rivera also acknowledges receipt of a fellowship from Iowa State University's Alliance for Graduate Education and the Professoriate (AGEP) program for underrepresented graduate students in STEM fields. The content of this paper however is solely the responsibility of the authors and does not represent the official views of either the NIBIB or the NIH.

believed [31] that the ability to understand noisy speech may be explained by the capacity of the brain for multisensory integration of input information, with the information coming in independently from the visual and the auditory modalities integrated to reduce noise and allow for more accurate perception [32], [33]. Recently, [31] studied the role of the superior temporal sulcus (STS) in the perception of noisy speech, through fMRI and behavioral experiments and established increased connectivity between the STS and the auditory or the visual cortex depending on whichever modality was more reliable, that is, less noisy.

[31] reported their fMRI analyses at the level of regions of interest (ROIs) drawn on the STS and the auditory and visual cortices. However, the full benefit of fMRI can be realized only if we are able to go beyond statements on functionality at the ROI level and delve into understanding cerebral function at the voxel level. Further, for using fMRI in a clinical setting, it may also be worthwhile to reliably detect activation at the voxel level and in single subjects. All these are potential scenarios with low CNRs where reliable activation detection methods are sorely needed. We return to this application in Section IV.

B. Background and Current Practices

Many thresholding methods [34]–[39] address the issue of multiple testing in determining significance of test statistics but generally ignore the spatial resolution of fMRI. This shortcoming is often accounted for by spatially smoothing the fMR images in the pre-processing stage, but such non-adaptive smoothing reduces both the adaptive spatial resolution and the number of available independent tests for detecting activation [40]. Iterative adaptive smoothing and segmentation methods in the form of propagation-separation (PS) [40] and adaptive-segmentation (AS) [41] have been developed. While operationally different, PS and AS are broadly similar, essentially yielding a segmentation of the SPM into activated and inactivated voxels. PS results (approximately) in a random t -field and uses Random Field Theory to segment the volume while AS uses multi-scale testing to determine activated segments. [41] argue for AS, because of its more general development and fewer model assumptions. AS also requires no heuristic corrections for spatial correlation, and attractively, provides decisions at prescribed significance levels. [41] demonstrated better performance of AS over PS in an auditory experiment. However, AS requires pre-specified bandwidth sequences and ignores correlation within the SPM. In this paper, we therefore develop a fully automated and computationally speedy adaptive smoothing and thresholding approach that accounts for correlation and obviates the need for setting any parameter beyond the significance level.

The remainder of this paper is organized as follows. In Section II, we provide theoretical and implementation details of our algorithm. We evaluate performance in a large-scale simulation experimental study in Section III. Both visual and numerical summaries of performance are presented. In Section IV, we illustrate applicability of our FAST algorithms on the dataset of Section I-A. We end with some discussion.

II. THEORY AND METHODS

A. Preliminaries

Let \mathbf{Y}_i be the time series vector of the observed BOLD response at the i th voxel obtained after preprocessing for registration and motion correction. A common approach relates \mathbf{Y}_i to the expected BOLD response via the general linear model

$$\mathbf{Y}_i = \mathbf{X}\boldsymbol{\beta}_i + \boldsymbol{\epsilon}_i, \quad (1)$$

where $\boldsymbol{\epsilon}_i$ is a p th-order auto-regressive (AR) Gaussian error vector with AR coefficients $\boldsymbol{\phi}_i = (\phi_{i1}, \phi_{i2}, \dots, \phi_{ip})$ and marginal variance σ_i^2 . Without loss of generality (w.l.o.g.), assume that the design matrix \mathbf{X} has the intercept in the first column, the expected BOLD response for the k stimulus levels in the next k columns, and polynomial terms for the drift parameter in the remaining m columns. Thus, $\boldsymbol{\beta}$ is a coefficient vector of length $d = k + m + 1$. We assume that the image volume has n voxels: thus $i = 1, 2, \dots, n$ in (1).

The parameters $(\hat{\beta}_i, \hat{\sigma}_i^2, \hat{\phi}_i)$ s are usually estimated via generalized least squares or restricted maximum likelihood. A typical analysis approach then applies (voxel-wise) hypothesis tests with the null hypothesis specifying no activation owing to the stimulus or task. SPMs of the form $\Gamma = \{c'\beta_i\}_{i \in V}$ with appropriate contrasts $c'\beta_i$ are then formulated at each voxel.

Many researchers use models that assume independence or AR(1) errors: others pre-whiten the time series before fitting (1) under independence. Incorrect model specifications can yield less precise SPMs [42]–[45]. In this paper, we used Bayes Information Criterion (BIC) [46], [47] which measures a fitted model's quality by trading its complexity against its fidelity to the data. Tests on the SPM Γ identify voxels that are activated related to the experiment. Specifically, voxel $i \in V$ is declared to be activated if a suitable test rejects the hypothesis $H_0: c'\beta_i = 0$ i.e., if $c'\hat{\beta}_i$ significantly deviates from zero. Our objective in this paper is to develop an approach that adaptively and automatically smooths and thresholds the SPM while accounting for the spatial correlation in the SPM and the fact that these sequence of thresholds yield SPMs from truncated distributions. Before detailing our algorithm, we provide some theoretical development.

B. Theoretical Development

We assume that the SPM is t -distributed with degrees of freedom large enough to be well-approximated via the standard normal distribution. We also assume a homogeneous correlation structure for the SPM, which is reasonable given our choice of a Gaussian kernel for smoothing. We have the

Theorem 1. *Let $\mathbf{X} \sim N_n(\mathbf{0}, \mathbf{R})$ where $\mathbf{X} = (X_1, \dots, X_n)'$ and \mathbf{R} is a circulant correlation matrix. Writing $\mathbf{1} = (1, 1, \dots, 1)'$, we let $\rho = \mathbf{R}^{-\frac{1}{2}}\mathbf{1}$ be the sum of the elements in the first row of $\mathbf{R}^{-\frac{1}{2}}$. Further, let $X_{(n)}$ be the maximum value of \mathbf{X} , that is, $X_{(n)} = \max\{X_1, X_2, \dots, X_n\}$. Then the cumulative distribution function (c.d.f.) $F_n(x)$ of $X_{(n)}$ is given by $F_n(x) = P(X_{(n)} \leq x) = [\Phi(\rho x)]^n$, where $\Phi(\cdot)$ is the c.d.f. of the standard normal random variable.*

Proof: From the definition of $X_{(n)}$, we have

$$\begin{aligned} F_n(x) &= P(\mathbf{X} \leq x\mathbf{1}) \\ &= P(\mathbf{R}^{-1/2}\mathbf{X} \leq x\mathbf{R}^{-1/2}\mathbf{1}) \\ &= P(\mathbf{Y} \leq \rho x\mathbf{1}), \text{ where } \mathbf{Y} \sim N_n(\mathbf{0}, \mathbf{I}_n) \\ &= P(Y_i \leq \rho x \quad \forall \quad i = 1, 2, \dots, n) = [\Phi(\rho x)]^n. \end{aligned} \tag{2}$$

■

In the limit, we are led to the following

Corollary 2. *Let \mathbf{X} and $X_{(n)}$ be as in Theorem 1. Then the limiting distribution of $X_{(n)}$ belongs to the domain of attraction of the Gumbel distribution, and satisfies:*

$$\lim_{n \rightarrow \infty} [F_n(a_n x + b_n)] = \exp\{e^{-x}\}, \tag{3}$$

where $a_n = \rho/[n\phi(b_n)]$ and $b_n = \Phi^{-1}(1 - 1/n)\rho$, with $\phi(\cdot)$ being the standard normal probability density function (p.d.f.).

Proof: For $\mathbf{Y} \sim N_n(\mathbf{0}, \mathbf{I}_n)$, the limiting distribution of $Y_{(n)}$ satisfies $\lim_{n \rightarrow \infty} [\Phi(a_n x + b_n)]^n = \exp\{e^{-x}\}$, with $a_n = 1/[n\phi(b_n)]$ and $b_n = \Phi^{-1}(1 - 1/n)$ [48]. The result follows from Theorem 1. ■

Theorem 1 and Corollary 2 provide the wherewithal for choosing a threshold using the limiting distribution of the maximum of correlated normal random variables with circulant correlation structure. Note however, that the first thresholding step results in *truncated* (and correlated) random variables that are under consideration for thresholding in subsequent steps. We account for this added complication by deriving the limiting distribution of the maximum of a correlated sample from a right-truncated normal

distribution. We do so by first noting that if Y_1, Y_2, \dots, Y_n are independent identically distributed random variables from the standard normal p.d.f truncated at η , then each Y_i has p.d.f. $\phi_\eta^\bullet(\cdot)$ and c.d.f. $\Phi_\eta^\bullet(\cdot)$:

$$\phi_\eta^\bullet(x) = \frac{\phi(x)}{\Phi(\eta)} I(x < \eta); \quad \Phi_\eta^\bullet(x) = \frac{\Phi(x)}{\Phi(\eta)} I(x < \eta). \quad (4)$$

Then $Y_{(n)} = \max\{Y_i, i = 1, 2, \dots, n\}$ has c.d.f. $G_\eta^\bullet(x) = [\Phi(x)/\Phi(\eta)]^n I(x < \eta)$ with limiting distribution given by

Theorem 3. *Let Y_1, Y_2, \dots, Y_n be a sample from (4). Then the limiting distribution of $Y_{(n)}$ belongs to the domain of attraction of the reverse Weibull distribution and satisfies*

$$\lim_{n \rightarrow \infty} [G_\eta^\bullet(a_n^\bullet x + b_n^\bullet)] = \exp\{-(-x^{-\tau})\} I(x \leq 0). \quad (5)$$

for some $\tau > 0$. Here $a_n^\bullet = \eta - \Phi_\eta^{\bullet-1}(1 - 1/n)$ and $b_n^\bullet = 0$.

Proof: Note that $\eta = \sup\{x \mid \Phi_\eta^\bullet(x) < 1\}$. From Theorem 10.5.2 in [49], a sufficient condition for $Y_{(n)}$ to be the domain of attraction is to demonstrate that

$$\lim_{x \rightarrow \eta} \frac{(\eta - x)\phi_\eta^\bullet(x)}{1 - \Phi_\eta^\bullet(x)} = \tau$$

for some $\tau > 0$ [50]. In our case, the limit holds because $\eta < \infty$. Then, using L'Hôpital's rule, we have

$$\begin{aligned} \lim_{x \rightarrow \eta} \frac{(\eta - x)\phi_\eta^\bullet(x)}{1 - \Phi_\eta^\bullet(x)} &= \lim_{x \rightarrow \eta} \frac{(\eta - x) \frac{d}{dx} \phi_\eta^\bullet(x) - \phi_\eta^\bullet(x)}{-\phi_\eta^\bullet(x)} \\ &= \lim_{x \rightarrow \eta} \frac{(\eta - x)\phi'(x)/\Phi(\eta) - \phi(x)/\Phi(\eta)}{-\phi(x)/\Phi(\eta)} \\ &= 1 \end{aligned}$$

Thus the right-truncated normal distribution satisfies the reverse Weibull condition and converges to the reverse Weibull distribution with $\tau \equiv 1$ in (5). The constants in the theorem are as per extreme value theory [48], [49]. ■

Theorem 4. *Let \mathbf{X} be a random vector from the $N_n(\mathbf{0}, \mathbf{R})$ density but that is right-truncated in each coordinate at η , with \mathbf{R} being a circulant correlation matrix. Let $\rho = \mathbf{R}^{-\frac{1}{2}} \mathbf{1}$ be the sum of the elements in the first row of $\mathbf{R}^{-\frac{1}{2}}$. Also, let $X_{(n)}$ be defined as before. Then the c.d.f. $F_\eta^\bullet(x)$ of $X_{(n)}$ is given by $F_\eta^\bullet(x) = P(X_{(n)} \leq x) = [\Phi(\rho x)/\Phi(\eta)]^n I(x < \eta)$.*

Proof: Proceeding as in the proof of Theorem 1 yields

$$\begin{aligned} F_\eta^\bullet(x) &= P(\mathbf{X} \leq x\mathbf{1}) \\ &= P(\mathbf{R}^{-1/2} \mathbf{X} \leq x\mathbf{R}^{-1/2} \mathbf{1}) \\ &= P(\mathbf{Y} \leq \rho x\mathbf{1}), \text{ where } Y_i \text{ s are i.i.d. } \Phi_{\rho\eta}^\bullet(y) \\ &= G_{\rho\eta}^\bullet(\rho x) = [\Phi(\rho x)/\Phi(\eta)]^n I(x < \eta). \end{aligned} \quad (6)$$

Corollary 5. *Let \mathbf{X} and $X_{(n)}$ be as in Theorem 4. Then the limiting distribution of $X_{(n)}$ belongs to the domain of attraction of the reverse Weibull distribution, and satisfies:*

$$\lim_{n \rightarrow \infty} [F_\eta^\bullet(a_n^\bullet x + b_n^\bullet)] = \exp\{-(-x^{-\alpha})\} I(x \leq 0). \quad (7)$$

where $a_n^\bullet = (\eta - \Phi_{\rho\eta}^{\bullet-1}(1 - 1/n))\rho$ and $b_n^\bullet = 0$.

Proof: From Theorem 3, the limiting distribution of Y_{nm} (5). Then $F_\eta^\bullet(x) = G_{\rho\eta}^\bullet(\rho x)$ from Theorem 4 and the result follows. ■

Having developed our results, we are now ready to propose our fast adaptive smoothing and thresholding algorithm.

C. Fast Adaptive Smoothing and Thresholding

Our proposed algorithm adaptively and, in sequence, smooths and identifies activated regions by thresholding. We estimate the amount of smoothing robustly or from the correlation structure, which we assume is well-approximated by a 3D Gaussian kernel. Thus, under the null hypothesis (of no activation anywhere), we assume that the SPM $\Gamma \sim N(\mathbf{0}, \mathbf{R})$ where $\mathbf{R} = \mathbf{S}_h$ with h the smoothing parameter of \mathbf{S}_h given in terms of its full-width-at-half-maximum. Let $\Gamma_{(-h)} \sim \mathbf{S}_h^{-\frac{1}{2}} \Gamma$. Then estimate h by maximizing the loglikelihood function

$$\ell(h \mid \Gamma_{(-h)}) = -\frac{n}{2} \log(2\pi) - \frac{1}{2} \log |\mathbf{S}_h| - \frac{1}{2} \Gamma'_{(-h)} \Gamma_{(-h)}. \quad (8)$$

Note that $\Gamma_{(-h)}$ and $|\mathbf{S}_h|$ are speedily computers using Fast Fourier transforms. Starting with the SPM Γ , obtained as discussed in Section II-A, we propose the algorithm:

- 1) *Initial Setup*. At this point, assume that $\zeta_i \equiv 0 \forall i$, where ζ_i is the activation status of the i th voxel. That is, assume that all voxels are inactive. Set $\zeta_i^{(0)} \equiv \zeta_i$. Also denote $\Gamma_{(0)} = \Gamma$, and $n_0 = n$, where n_k denotes the number of voxels for which $\zeta_i^{(k)} = 0$.
- 2) *Iterative Steps*. For $k=1, 2, \dots$, iterate as follows:
 - a) *Smoothing*. We smooth $\Gamma_{(k-1)}$ in one of two ways:
 - i) *Adaptive Maximum Likelihood (AM-FAST, pronounced äm-fast)*: Maximize (8) given $\Gamma_{(k-1)}$ to obtain h_k . Obtain $\Gamma_{(k)}$ by smoothing $\Gamma_{(k-1)}$ with \mathbf{S}_{h_k} . Also obtain $\rho_k = \mathbf{S}_{h_k}^{-\frac{1}{2}} \mathbf{1}$.
 - ii) *Adaptive Robust Smoothing (AR-FAST, pronounced ahr-fast)*: Use robust methods [51] on $\Gamma_{(k-1)}$ to get $\Gamma_{(k)}$. Now, maximize (8) given $\Gamma_{(k)}$ to obtain h_k and $\rho_k = \mathbf{S}_{h_k}^{-\frac{1}{2}} \mathbf{1}$.
 - b) *Adaptive Thresholding*. This consists of two steps:
 - i) For $k=1$, use Corollary 2 to obtain a_n and b_n , otherwise (*i.e.* for $k > 1$) use Corollary 5 to obtain $a_{n_{k-1}}^\bullet$. In both cases, we use the spatial correlation estimated by $\mathbf{S}_{h_{k-1}}$.
 - ii) From the Gumbel (for $k=1$) or reverse Weibull distributions (for $k > 1$), get

$$\eta_k = \begin{cases} a_{n_0} \iota_\alpha^{\mathcal{G}} + b_{n_0} & \text{for } k=1 \\ a_{n_{k-1}}^\bullet \iota_\alpha^{\mathcal{W}} & \text{otherwise.} \end{cases} \quad (9)$$

where $\iota_\alpha^{\mathcal{G}}$ and $\iota_\alpha^{\mathcal{W}}$ are the upper-tail α -values for the Gumbel and the reverse Weibull (with $\tau=1$) distributions, respectively.

- iii) Set all $\zeta_i^{(k)} = 1$ if $\zeta_i^{(k-1)} = 0$ and if the i th coordinate of $\Gamma_{(k)}$ exceeds η_k . Also, update $n_k = \sum_{i=1}^n \zeta_i^{(k)}$.

- 3) *Stopping criterion*. Let $J(\zeta^{(k)}, \zeta^{(k-1)})$, be the Jaccard Index [52], [53] of the activation maps in successive iterations (*i.e.* between the $(k-1)$ th and k th iterations). If $J(\zeta^{(k)}, \zeta^{(k-1)}) \leq J(\zeta^{(k+1)}, \zeta^{(k)})$, then the algorithm terminates and $\zeta^{(k)}$ is the final activation map.

Comments: A few comments are in order:

a) *Two-sided tests*: Our development here assumes one-sided tests where (w.l.o.g.) large values are the extremal values of the SPM. Two-sided tests can be easily accommodated by simply replacing the α in (9) by $\alpha/2$ and by using the absolute value of the components of $\Gamma_{(k)}$ to decide on activation.

b) *Comparison with AS*: AS [41] also provides an adaptive weighted smoothing approach based on multi-scale testing. Both AM-FAST and AR-FAST have similarities with AS, in that they also smooth and threshold iteratively. However, there are a few fundamental differences. For one, the AS approach has a set user-specified sequence of bandwidths that smooths $\Gamma_{(k)}$ at each step. In contrast, we use likelihood maximization (for AM-FAST) or robust (for AR-FAST) methods to optimally determine h at each step. AS also performs thresholding in a similar manner as us, but they use a general Fréchet extreme value distribution. Their development ignores both the spatial context and also the fact that thresholding results in subsequent truncated decisions. Our development represents the procedure more accurately because

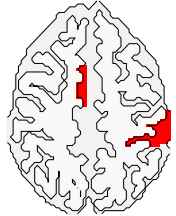
we account for both the correlation structure (resulting in the initial cut-off decided as per the Gumbel distribution) and the truncation (with the subsequent cut-offs being determined by the reverse Weibull distribution). Finally, our method is completely data-driven, with termination declared only when the Jaccard index indicates no substantial changes in the detected activation.

III. PERFORMANCE EVALUATIONS

This section reports performance of the FAST algorithm relative to the AS and also the more popular cluster-thresholding algorithms. We use a 2D setup to make it computationally possible to evaluate performance across many settings.

A. Experimental Setup

Our simulation setup was a modified version of the digitized 128×128 2D Hoffman phantom [54] often used in Positron Emission Tomography. The phantom (Figure 1) has 3465 in-brain pixels, representing two types (say, A and B) of anatomic structures. 138 of the B-type pixels from two contiguous regions were deemed to be truly activated. The phantom provided the values (see Figure 1) for $\beta_i = (\beta_{i0}, \beta_{i1}, \beta_{i2})$



Region	β_{i0}	β_{i1}	β_{i2}
Background	0	0	0
Brain A	4500	0	-155.32
Brain B	6000	0	-155.32
Activated	6000	600	-155.32

Fig. 1: The phantom used in our simulation experiments. Putative anatomic regions (A and B) are in shades of grey, while truly activated pixels are in red. The table on the right lists the β_i s used in our simulations.

in (1) as per the location of the i th pixel in the phantom.

As in (1), the design matrix \mathbf{X} had the intercept in the first column. For the second column, the input stimulus time series was set to alternate as 16 on-off blocks of 6 time-points each. The first block signaled rest, with input stimulus 0, while the second block was 1 to signify activation. These blocks alternated, yielding values at 96 time-points. These temporal values were convolved with the hemodynamic response function [7] to provide the second column of \mathbf{X} . The third column of \mathbf{X} represented linear drift and was set to t ($t = 1, 2, \dots, 96$). Also, as per (1), AR(p) errors were simulated for different p and for different structures. Specifically, for each p , we considered AR coefficients for a range of $\phi \equiv \phi_i$ s with coefficients $(\phi_1, \phi_2, \dots, \phi_p)$ that were, with lag, (a) all equal, (b) decreasing, (c) increasing, (d) first decreasing and then increasing and (e) first increasing and then decreasing. To ensure stationary solutions, we restricted $\sum_{j=1}^p \phi_j = 0.9$. Thus, for AR(1), we have $\phi_1 \equiv 0.9$ for all cases. For $p = 2, 3, 4$, we have $\phi_i \equiv 0.9/p$ for the equal AR coefficients scenario. Table I contains the ϕ -values for the other cases. Finally, we chose σ to be such that they corresponded to very low to moderate CNR settings. Specifically, we set $\sigma_0 = 240, 300, 400$ yielding $\text{CNR} = 1.0, 1.5$, and 2.0 . By design, our SNRs were 10 times our CNRs.

We simulated realizations of time series images using (1) and the setup of Figure 1 and the AR structures in Table I. For each pixel, we fitted (1) with different AR(p), $p = 0, 1, 2, 3, 4, 5$, and chose the model that provided the minimum BIC. SPMs were generated as discussed in Section II-A. Figure 2 provides sample realizations of SPMs obtained using our simulation setup and using AR(4) time series. We also performed a larger-scale simulation study, where we replicated our experiment 25 times for each simulation setting. Activation detection was done with AM-FAST and AR-FAST and also the commonly-used (in fMRI) cluster-thresholding (CT) at [39]’s suggested significance level ($\alpha = 0.001$) with a second-order neighborhood and number of voxels determined by [55]’s `3dClustSim` function. The R package

TABLE I: ϕ s for the AR(p) scenarios used in our simulations.

p	Decreasing	Increasing
2	(0.6, 0.3)	(0.3, 0.6)
3	(0.4, 0.3, 0.2)	(0.2, 0.3, 0.4)
4	(0.3, 0.25, 0.20, 0.15)	(0.15, 0.20, 0.25, 0.3)
5	(0.3, 0.25, 0.20, 0.10, 0.05)	(0.05, 0.10, 0.20, 0.25, 0.30)
p	Decreasing-Increasing	Increasing-Decreasing
2	(0.6,0.3)	(0.3,0.6)
3	(0.4,0.1,0.4)	(0.1,0.7,0.1)
4	(0.4,0.05,0.05,0.4)	(0.05,0.4,0.4,0.05)
5	(0.25,0.15,0.1,0.15,0.25)	(0.1,0.15,0.4,0.15,0.1)

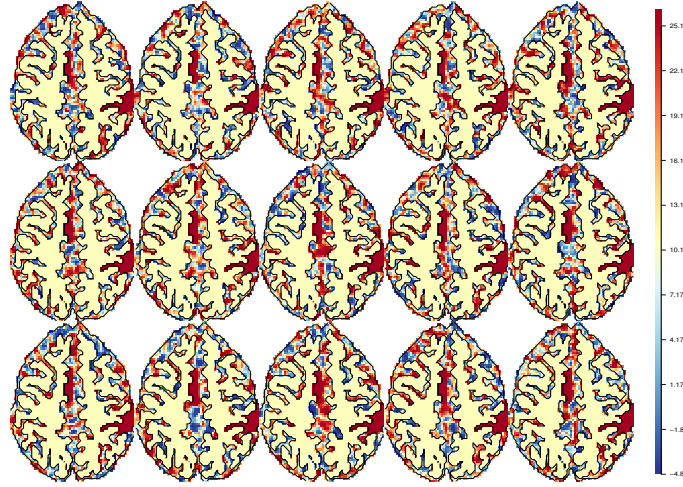


Fig. 2: SPM for a sample simulation setting, for the five settings (from left to right) of equal, increasing, decreasing, increasing-decreasing and decreasing-increasing AR coefficients. The three rows (from top to bottom) correspond to simulation settings with CNR of 1.0, 1.5 and 2.0, respectively.

AnalyzeFMRI [56] was used to perform cluster-wise thresholding. We also performed AS [41] (henceforth, TP11) using the R package `fmri` [57]. In each case, performance was evaluated in terms of the Jaccard Index [52], [53] between the estimated activation map and the truth as per Figure 1.

B. Results

Figure 3 provides activation maps detected using AM-FAST (with $\alpha = 0.025$), CT and TP11 for each case of Figure 2. AR-FAST results were essentially indistinguishable from AM-FAST and so are not displayed. It is encouraging to note that AM-FAST visually tracks very closely to the activation regions of Figure 1. Both CT and TP11 also identify the true regions as activated but they also identify several other pixels as activated, with more false positives detected at lower CNR levels. At moderate CNR=2.0, CT does very well under the equal AR coefficients case but not as well as for some of the other cases. TP11 however has more false positives even for CNR=2.0. In summary, however, AM-FAST performs quite creditably at all CNR levels.

Figure 4 displays performance of our algorithms and its competitors in the large-scale simulation study. For low CNRs, both CT and TP11 perform poorly, but AM-FAST and AR-FAST perform quite well. As with Figure 3, both CT and TP11 improve with increased CNR: indeed CT is marginally the best performer for when CNR=2.0 and with no autocorrelation ($p = 0$). Interestingly, for CNR=2.0, CT does worse than AM-FAST or AR-FAST for the decreasing AR coefficients case but not necessarily for the other cases. AM-FAST and AR-FAST perform very similarly at all settings, however AM-FAST is computationally faster than AR-FAST. The poorer performance of CT relative to the FAST algorithms is not surprising because `3dClustSim` and other such functions are not very adaptive in their execution. TP11 is however,

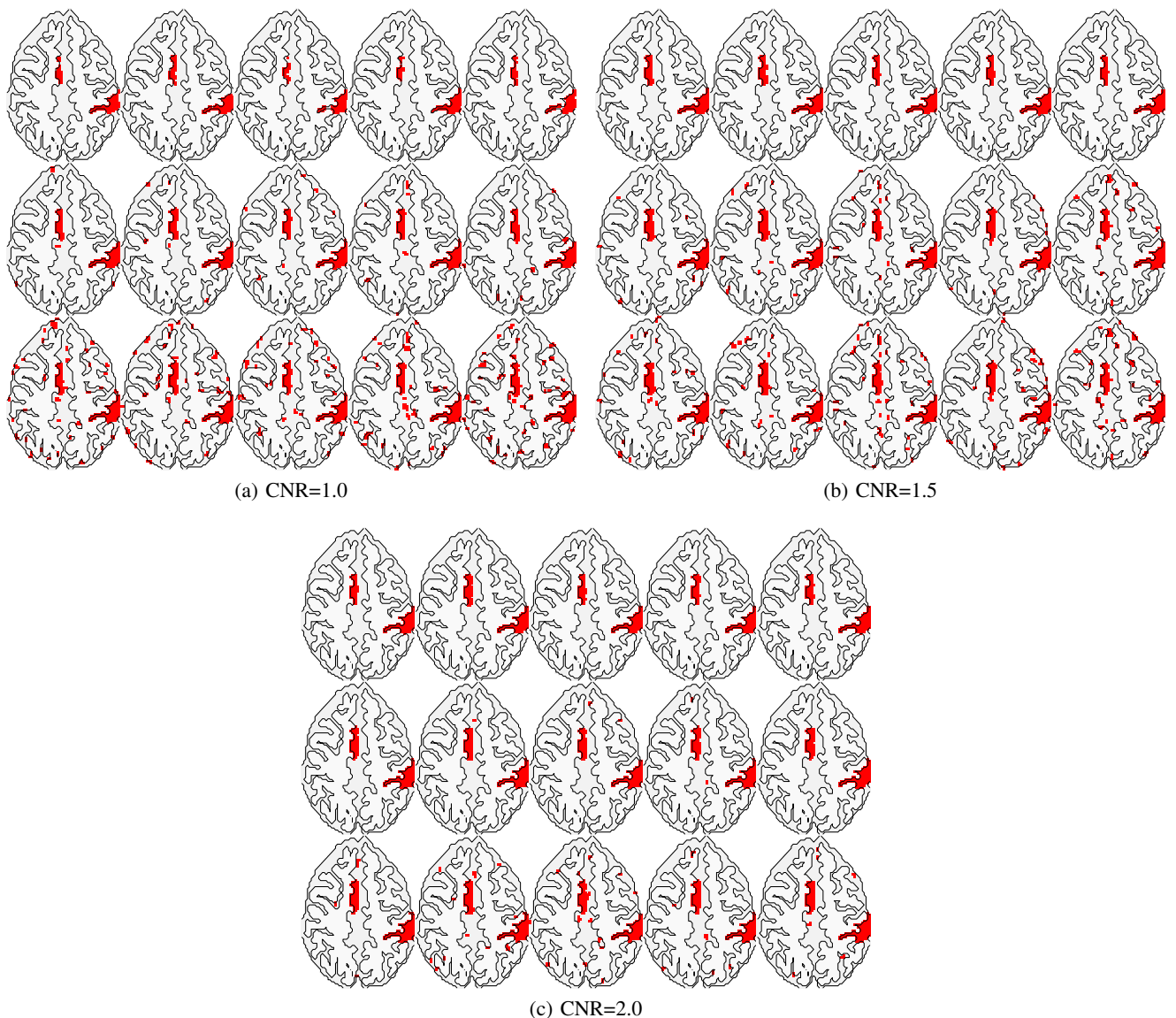


Fig. 3: Activation maps obtained using AM-FAST (top row), CT (middle) and TP11 (bottom row) from the SPMs of Figure 2 at each CNR. Columns are as in Figure 2.

somewhat more adaptive, through the choice of the sequence of smoothing parameters that is left to the user. Specifying this sequence appropriately may, however, require considerable skill, and the default values provided in the `fMRI` package do not appear to be adequate enough for lower CNR situations. On the other hand, our approach determines the optimal smoothing from the SPM at each iteration through likelihood maximization (AM-FAST) or robust methods (AR-FAST). Interestingly though, we have found that α plays a role in the FAST algorithms with smaller values performing marginally better with higher CNRs and higher values performing substantially better for lower CNRs. As a via media, we use $\alpha = 0.025$ in our application. In summary, however, both FAST algorithms perform very well and over a wide range of low-to-moderate CNR settings.

IV. ACTIVATION DURING PERCEPTION OF NOISY SPEECH

The dataset is from [31] and also provided by [55] as `data6` to illustrate the many features of the AFNI software. In this experiment the subject was presented with audiovisual speech in both auditory and visual formats. There were two types of stimuli: (1) audio-reliable where the subject could clearly hear the

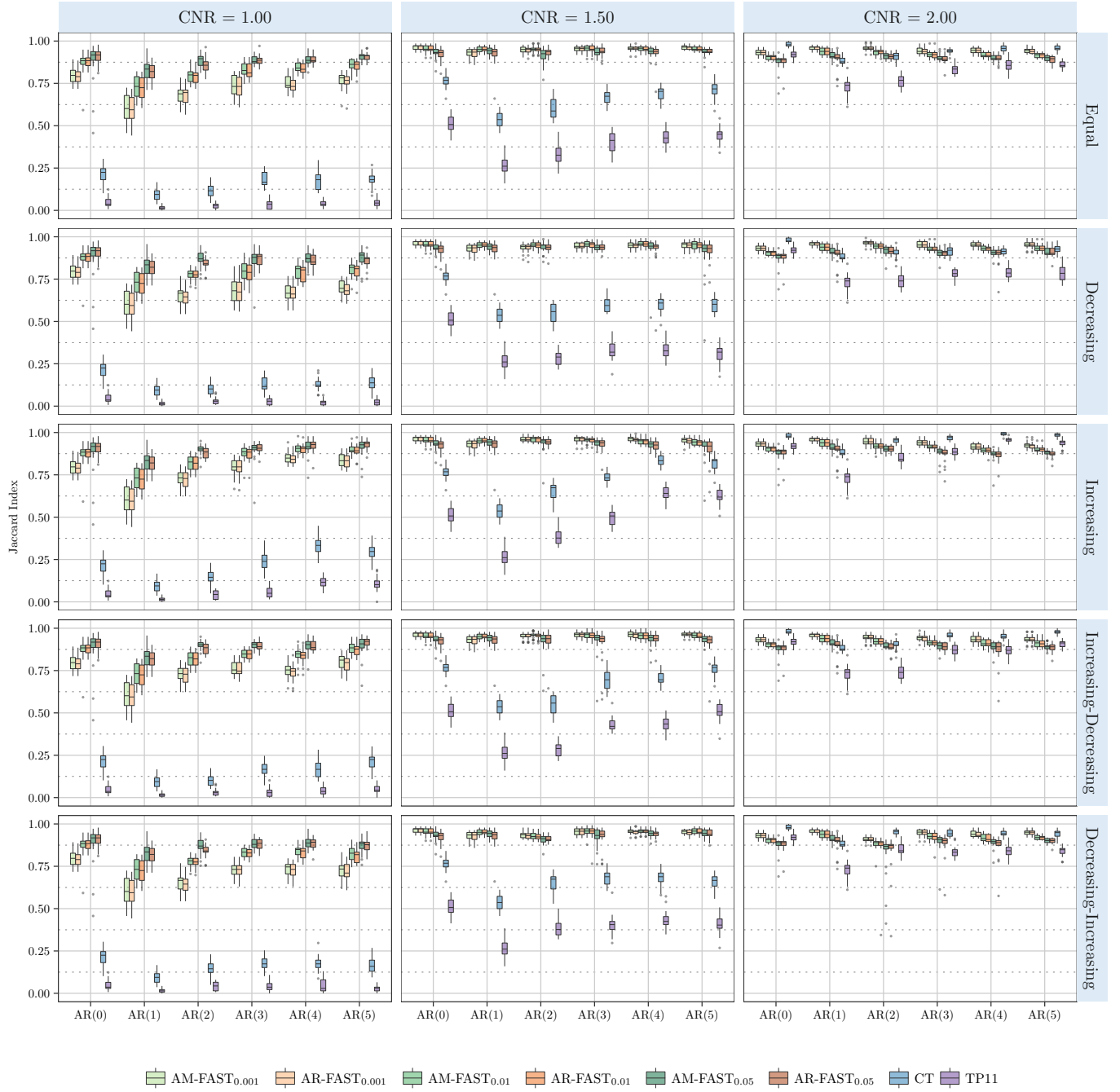


Fig. 4: Summary of performance of the AM-FAST, AR-FAST, CT and TP11 algorithms for the different simulation settings. The subscript on the FAST legends represents the value of $\alpha = 0.001, 0.01, 0.05$ used in the experiments.

spoken word but the visual of the female speaker was degraded and (2) visual-reliable where the subject could clearly see the female speaker vocalizing the word but the audio was of reduced quality. There were three experimental runs, each consisting of a randomized design of 10 blocks, equally divided into blocks of audio-reliable and visual-reliable stimuli. An echo-planar imaging sequence ($TR=2s$) was used to obtain T_2^* -weighted images with volumes of $80 \times 80 \times 33$ (voxel dimensions = $2.75 \times 2.75 \times 3.0 \text{ mm}^3$) over 152 time-points. Our goal was to determine activation in areas that responded to the audio task ($H_0 : \beta_a = 0$), areas that responded to the visual task ($H_0 : \beta_v = 0$) and finally the contrast of visual

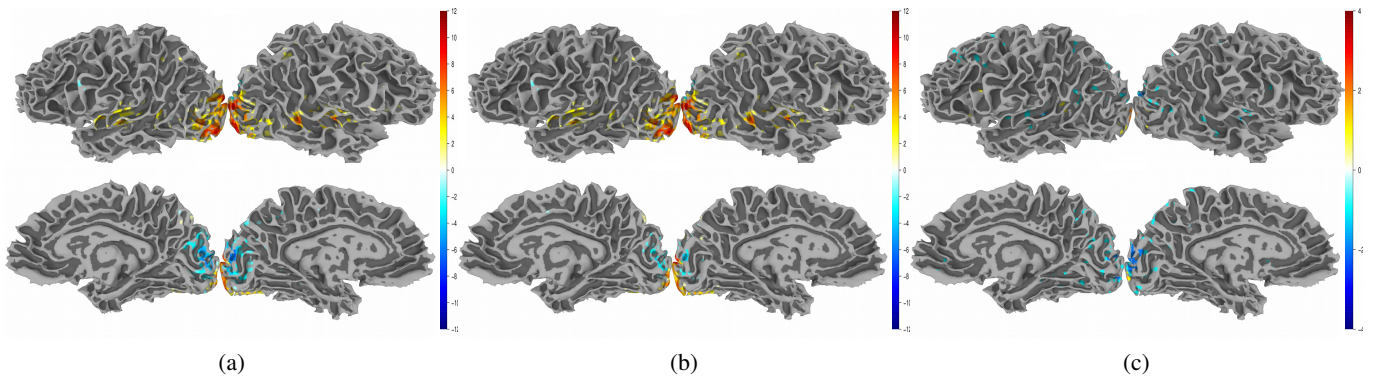


Fig. 5: Activation regions in *AFNI data6* using SPM based on $AR(\hat{p})$ of (a) Visual-reliable stimulus (b) Audio-reliable stimulus and (c) the difference contrast between Visual-reliable and Audio-reliable stimuli.

against audio ($H_0 : \beta_v - \beta_a = 0$). We fitted AR models at each voxel using $p = 0, 1, 2, 3, 4, 5$ and chose p minimizing the BIC. After obtaining the SPM, we applied AM-FAST with results displayed via AFNI and Surface Mapping (SUMA) in Figure 5. Note that most of the activation occurs in Brodmann areas 18 and 19 (BA18 and BA19), which comprise the occipital cortex and the extrastriate (or peristriate) cortex. In humans with normal sight, extrastriate cortex is a visual association area, where feature-extraction, shape recognition, attentional, and multimodal integrating functions take place. We also observed activated regions in superior temporal sulcus (STS). Recent studies have shown increased activation in this area which are related to: voices versus environmental sounds, stories versus nonsensical speech, moving faces versus moving objects, biological motion and so on [58]. Although a detailed analysis of the results of this study is beyond the purview of this paper, we note that AM-FAST finds interpretable results even when applied to a single subject high-level cognition experiment.

V. DISCUSSION

In this paper, we have proposed a new fully automated and adaptive smoothing and thresholding algorithm called FAST that has the ability to perform activation detection in a range of low-signal regions. Two variants AM-FAST and AR-FAST, have been proposed that show similar performance. We recommend AM-FAST because it is computationally faster than AR-FAST. Our methodology accounts for both spatial correlation structure and uses more accurate extreme value theory in its development. Simulation experiments indicate good performance over a range of low-SNR and low-CNR settings. Developing FAST for more sophisticated time series and spatial models, as well as increased use of diagnostics in understanding activation and cognition are important research areas and directions that would benefit from further attention.

REFERENCES

- [1] J. W. Belliveau, D. N. Kennedy, R. C. McKinstry, B. R. Buchbinder, R. M. Weisskoff, M. S. Cohen, J. M. Vevea, T. J. Brady, and B. R. Rosen, "Functional mapping of the human visual cortex by magnetic resonance imaging," *Science*, vol. 254, pp. 716–719, 1991.
- [2] K. K. Kwong, J. W. Belliveau, D. A. Chesler, I. E. Goldberg, R. M. Weisskoff, B. P. Poncelet, D. N. Kennedy, B. E. Hoppel, M. S. Cohen, R. Turner, H.-M. Cheng, T. J. Brady, and B. R. Rosen, "Dynamic magnetic resonance imaging of human brain activity during primary sensory stimulation," *Proceedings of the National Academy of Sciences of the United States of America*, vol. 89, pp. 5675–5679, 1992.
- [3] P. A. Bandettini, A. Jesmanowicz, E. C. Wong, and J. S. Hyde, "Processing strategies for time-course data sets in functional MRI of the human brain," *Magnetic Resonance in Medicine*, vol. 30, pp. 161–173, 1993.
- [4] K. J. Friston, A. P. Holmes, K. J. Worsley, J.-B. Poline, C. D. Frith, and R. S. J. Frackowiak, "Statistical parametric maps in functional imaging: A general linear approach," *Human Brain Mapping*, vol. 2, pp. 189–210, 1995.
- [5] A. M. Howseman and R. W. Bowtell, "Functional magnetic resonance imaging: imaging techniques and contrast mechanisms," *Philosophical Transactional of the Royal Society, London*, vol. 354, pp. 1179–94, 1999.

- [6] W. D. Penny, K. J. Friston, J. T. Ashburner, S. J. Kiebel, and T. E. Nichols, Eds., *Statistical Parametric Mapping: The Analysis of Functional Brain Images*, 1st ed. Academic Press, 2006.
- [7] M. A. Lindquist, "The statistical analysis of fMRI data," *Statistical Science*, vol. 23, no. 4, pp. 439–464, 2008.
- [8] N. A. Lazar, *The Statistical Analysis of Functional MRI Data*. Springer, 2008.
- [9] F. G. Ashby, *Statistical Analysis of fMRI Data*. MIT Press, 2011.
- [10] S. Ogawa, T. M. Lee, A. S. Nayak, and P. Glynn, "Oxygenation-sensitive contrast in magnetic resonance image of rodent brain at high magnetic fields," *Magnetic Resonance in Medicine*, vol. 14, pp. 68–78, 1990.
- [11] S. Ogawa, T. M. Lee, A. R. Kay, and D. W. Tank, "Brain magnetic resonance imaging with contrast dependent on blood oxygenation," *Proceedings of the National Academy of Sciences, USA*, vol. 87, no. 24, pp. 9868–9872, 1990.
- [12] K. J. Worsley, C. H. Liao, J. Aston, V. Petre, G. H. Duncan, F. Morales, and A. C. Evans, "A general statistical analysis for fmri data," *NeuroImage*, vol. 15, pp. 1–15, 2002.
- [13] K. J. Friston, P. Fletcher, O. Josephs, A. Holmes, M. Rugg, and R. Turner, "Event-related fMRI: characterizing differential responses," *Neuroimage*, vol. 7, no. 1, pp. 30–40, 1998.
- [14] G. H. Glover, "Deconvolution of impulse response in event-related bold fmri," *NeuroImage*, vol. 9, pp. 416–429, 1999.
- [15] R. B. Buxton, K. Uludağ, D. J. Dubowitz, and T. T. Liu, "Modeling the hemodynamic response to brain activation," *Neuroimage*, vol. 23, pp. S220–S233, 2004.
- [16] K. J. Friston, C. D. Frith, P. F. Liddle, R. J. Dolan, A. A. Lammertsma, and R. S. J. Frackowiak, "The relationship between global and local changes in PET scans," *Journal of Cerebral Blood Flow and Metabolism*, vol. 10, pp. 458–466, 1990.
- [17] K. J. Friston, A. P. Holmes, K. J. Worsley, J.-P. Poline, C. D. Frith, and R. S. Frackowiak, "Statistical parametric maps in functional imaging: a general linear approach," *Human brain mapping*, vol. 2, no. 4, pp. 189–210, 1994.
- [18] K. J. Worsley and K. J. Friston, "Analysis of fMRI time-series revisited again," *Neuroimage*, vol. 2, no. 3, pp. 173–181, 1995.
- [19] C. R. Genovese, N. A. Lazar, and T. Nichols, "Thresholding of statistical maps in functional neuroimaging using the false discovery rate," *Neuroimage*, vol. 15, no. 4, pp. 870–878, 2002.
- [20] J. V. Hajnal, R. Myers, A. Oatridge, J. E. Schweiso, J. R. Young, and G. M. Bydder, "Artifacts due to stimulus-correlated motion in functional imaging of the brain," *Magnetic Resonance in Medicine*, vol. 31, pp. 283–291, 1994.
- [21] B. Biswal, A. E. DeYoe, and J. S. Hyde, "Reduction of physiological fluctuations in fMRI using digital filters," *Magnetic Resonance in Medicine*, vol. 35, no. 1, pp. 107–113, January 1996. [Online]. Available: <http://view.ncbi.nlm.nih.gov/pubmed/8771028>
- [22] R. P. Wood, S. T. Grafton, J. D. G. Watson, N. L. Sicutte, and J. C. Mazziotta, "Automated image registration. ii. intersubject validation of linear and non-linear models," *Journal of Computed Assisted Tomography*, vol. 22, pp. 253–265, 1998.
- [23] R. P. Gullapalli, R. Maitra, S. Roys, G. Smith, G. Alon, and J. Greenspan, "Reliability estimation of grouped functional imaging data using penalized maximum likelihood," *Magnetic Resonance in Medicine*, vol. 53, pp. 1126–1134, 2005.
- [24] R. Maitra, S. R. Roys, and R. P. Gullapalli, "Test-retest reliability estimation of functional mri data," *Magnetic Resonance in Medicine*, vol. 48, pp. 62–70, 2002.
- [25] R. Maitra, "Initializing partition-optimization algorithms," *IEEE/ACM Transactions on Computational Biology and Bioinformatics*, vol. 6, pp. 144–157, 2009. [Online]. Available: <http://doi.ieeecomputersociety.org/10.1109/TCBB.2007.70244>
- [26] Z. S. Saad, D. R. Glen, G. Chen, M. S. Beauchamp, R. Desai, and R. W. Cox, "A new method for improving functional-to-structural mri alignment using local pearson correlation," *NeuroImage*, vol. 44, pp. 839–848, 2009.
- [27] E. E. Chen and S. L. Small, "Test-retest reliability in fMRI of language: Group and task effects," *Brain and Language*, vol. 102, no. 2, pp. 176–85, 2007. [Online]. Available: <http://dx.doi.org/10.1016/j.bandl.2006.04.015>
- [28] K. D. Kryter, *The handbook of hearing and the effects of noise: Physiology, psychology, and public health*. Academic Press, 1994.
- [29] M. D. Hauser, *The evolution of communication*. MIT press, 1996.
- [30] S. Dupont and J. Luetin, "Audio-visual speech modeling for continuous speech recognition," *IEEE transactions on multimedia*, vol. 2, no. 3, pp. 141–151, 2000.
- [31] A. R. Nath and M. S. Beauchamp, "Dynamic changes in superior temporal sulcus connectivity during perception of noisy audiovisual speech," *The Journal of Neuroscience*, vol. 31, no. 5, p. 1704 1714, 2011.
- [32] W. H. Sumby and I. Pollack, "Visual contribution to speech intelligibility in noise," *The journal of the acoustical society of america*, vol. 26, no. 2, pp. 212–215, 1954.
- [33] B. E. Stein and M. A. Meredith, *The merging of the senses*. The MIT Press, 1993.
- [34] Y. Benjamini, A. M. Krieger, and D. Yekutieli, "Adaptive linear step-up procedures that control the false discovery rate," *Biometrika*, vol. 93, no. 3, pp. 491–507, 2006.
- [35] R. Heller, D. Stanley, D. Yekutieli, N. Rubin, and Y. Benjamini, "Cluster-based analysis of fMRI data," *NeuroImage*, vol. 33, no. 2, pp. 599–608, Nov. 2006. [Online]. Available: <http://dx.doi.org/10.1016/j.neuroimage.2006.04.233>
- [36] Y. Benjamini and R. Heller, "False discovery rates for spatial signals," *Journal of the American Statistical Association*, vol. 102, no. 480, pp. 1272–1281, 2007.
- [37] M. Smith and L. Fahrmeir, "Spatial Bayesian variable selection with application to functional Magnetic Resonance Imaging," *Journal of the American Statistical Association*, vol. 102, no. 478, pp. 417–431, 2007. [Online]. Available: <http://pubs.amstat.org/doi/abs/10.1198/016214506000001031>
- [38] S. M. Smith and T. E. Nichols, "Threshold-free cluster enhancement: Addressing problems of smoothing, threshold dependence and localisation in cluster inference," *Neuroimage*, vol. 44, pp. 83–98, 2009.
- [39] C.-W. Woo, A. Krishnan, and T. D. Wager, "Cluster-extent based thresholding in fMRI analyses: Pitfalls and recommendations," *Neuroimage*, vol. 91, p. 412419, 2014.
- [40] K. Tabelow, J. Polzehl, H. U. Voss, and V. Spokoiny, "Analyzing fMRI experiments with structural adaptive smoothing procedures," *NeuroImage*, vol. 33, no. 1, pp. 55–62, 2006.
- [41] J. Polzehl, H. U. Voss, and K. Tabelow, "Structural adaptive segmentation for statistical parametric mapping," *NeuroImage*, vol. 52, no. 2, pp. 515–523, 2010.

- [42] M. M. Monti, "Statistical analysis of fMRI time-series: A critical review of the glm approach," *Frontiers in Human Neuroscience*, vol. 5, no. 00028, pp. 1–13, 2011. [Online]. Available: http://www.frontiersin.org/Journal/Abstract.aspx?s=537&name=human_neuroscience&ART_Doi=10.3389/fnhum.2011.00028
- [43] W.-L. Luo and T. E. Nichols, "Diagnosis and exploration of massively univariate neuroimaging models," *Neuroimage*, vol. 19, no. 3, pp. 1014–1032, 2003.
- [44] J. M. Loh, M. A. Lindquist, and T. D. Wager, "Residual analysis for detecting mis-modeling in fMRI," *Statistica Sinica*, pp. 1421–1448, 2008.
- [45] M. Lindquist, J. Loh, L. Atlas, and T. Wager, "Modeling the hemodynamic response function in fMRI: Efficiency, bias and mis-modeling," *Neuroimage*, vol. 45, no. 1, p. S187S196, 2009.
- [46] G. Schwarz, "Estimating the dimensions of a model," *Annals of Statistics*, vol. 6, pp. 461–464, 1978.
- [47] R. H. Shumway and D. S. Stoffer, *Time Series Analysis and Its Applications*, second edition ed. Springer, 2006.
- [48] S. I. Resnick, *Extreme values, regular variation and point processes*. Springer, 2013.
- [49] H. A. David and H. N. Nagaraja, *Order Statistics*. Hoboken, New Jersey: John Wiley and Sons, Inc., 2003.
- [50] R. Von Mises, "La distribution de la plus grande de n valeurs," *Rev. math. Union interbalcanique*, vol. 1, no. 1, 1936.
- [51] D. Garcia, "Robust smoothing of gridded data in one and higher dimensions with missing values," *Computational statistics & data analysis*, vol. 54, no. 4, pp. 1167–1178, 2010.
- [52] P. Jaccard, "Étude comparative de la distribution florale dans une portion des alpes et des jura," *Bulletin del la Société Vaudoise des Sciences Naturelles*, vol. 37, p. 547579, 1901.
- [53] R. Maitra, "A re-defined and generalized percent-overlap-of-activation measure for studies of fMRI reproducibility and its use in identifying outlier activation maps," *Neuroimage*, vol. 50, no. 1, pp. 124–135, 2010.
- [54] E. J. Hoffman, P. D. Cutler, W. M. Digby, and J. C. Mazziotta, "3-d phantom to simulate cerebral blood flow and metabolic images for pet," *IEEE Transactions on Nuclear Science*, vol. 37, pp. 616–620, 1990.
- [55] R. W. Cox, "Afni: software for analysis and visualization of functional magnetic resonance neuroimages," *Computers and Biomedical research*, vol. 29, no. 3, pp. 162–173, 1996.
- [56] C. Bordier, M. Dojat, and P. L. de Micheaux, "Temporal and spatial independent component analysis for fmri data sets embedded in the AnalyzeFMRI R package," *Journal of Statistical Software*, vol. 44, no. 9, pp. 1–24, 2011. [Online]. Available: <http://www.jstatsoft.org/v44/i09/>
- [57] K. Tabelow and J. Polzehl, "Statistical parametric maps for functional mri experiments in R: The package fmri," *Journal of Statistical Software*, vol. 44, no. 11, pp. 1–21, 2011. [Online]. Available: <http://www.jstatsoft.org/v44/i11/>
- [58] E. Grossman and R. Blake, "Brain activity evoked by inverted and imagined biological motion," *Vision research*, vol. 41, no. 10, pp. 1475–1482, 2001.